Modeling, Simulation and Control of Turboelectric Propulsion Systems for More Electric Aircraft using Modelica

Marcelo de Castro*, Luigi Vanfretti †
Rensselaer Polytechnic Institute, Troy, NY, 12180

Yebin Wang ‡, Hongyu Wang§, Dehong Liu ¶, Scott Bortoff ‖
Mitsubishi Electric Research Laboratories, Cambridge, MA, 02139

Tomoki Takegami**
Mitsubishi Electric Corporation, Amagasaki City, Japan

As aviation industry moves towards More Electric Aircraft technologies, electrification of non-propulsive loads is becoming more common. Moreover, new designs for electrified propulsive systems have been proposed in the literature, drawing attention from the aviation sector. Amidst the proposed topologies, turboelectric architectures present a set of benefits, becoming attractive for more electric powertrains. Given this context, this paper presents Modelica as the means for developing models to assess the dynamic performance for the different possible turboelectric architectures that can be adopted by industry in the next few years. Individual components have their mathematical models presented along with their respective Modelica implementation. Two different possible architectures are assembled using the Modelica models and their dynamic performances over a 400-second sample flight mission are assessed. The dynamic simulations provide insights for choosing system's parameters, controllers' design and system sizing.

I. Nomenclature

MEA	=	More Electric Aircraft
EAP	=	Electrified Aircraft Propulsion
BLI	=	Boundary Layer Injection
$PMSG$	=	Permanent Magnet Synchronous Generator
$FCSG$	=	Field Controlled Synchronous Generator
$PMSM$	=	Permanent Magnet Synchronous Motor
AC	=	Alternating Current
DC	=	Direct Current
MSL	=	Modelica Standard Library
VSC	=	Voltage Source Converter
CSD	=	Constant Speed Drive
$VSVF$	=	Variable Speed Variable Frequency
VSI	=	Voltage Source Inverter
rpm	=	Rotations Per Minute
$IGBT$	=	Insulated-Gate Bipolar Transistor

*Doctorate Candidate, Department of Electrical Computer and Systems Engineering, Rensselaer Polytechnic Institute
†Associate Professor, Department of Electrical Computer and Systems Engineering, Rensselaer Polytechnic Institute.
‡Senior Principal Research Scientist, Multi-Physics & Dynamics Group, Mitsubishi Electric Research Laboratories.
§Visiting Research Scientist, Multi-Physics & Dynamics Group, Mitsubishi Electric Research Laboratories.
¶Senior Principal Research Scientist, Multi-Physics & Dynamics Group, Mitsubishi Electric Research Laboratories.
‖Strategic Project Leader and Chief Scientist, Multi-Physical Systems Group, Mitsubishi Electric Research Laboratories.
**Advanced Technology R&D Center, Mitsubishi Electric Corporation

II. Introduction

A. Background

INCREASING growth in global environmental concerns has made it evident that substantial cuts in Greenhouse Gas emissions from the transportation sector are needed. In this context, the aviation industry, a contributor of roughly 2.1% of total human-induced CO2 emissions, has continuously developed advanced energy-efficient solutions to diminish its environmental impact. In fact, important progress has been made during the past decades to move towards More Electric Aircraft (MEA) designs [1].

The main goal of moving into MEAs is to transform any non-propulsive load in an airplane to be fed by the electrical power system of the aircraft. Increasing aircraft electrification is envisioned to bring in benefits such as higher efficiency, controllability and reconfigurability to the aircraft's components, while facilitating maintenance procedures [2]. This set of advantages is easily translated into economic benefits.

In addition to electrification of non-propulsive loads, different architectures for Electrified Aircraft Propulsion (EAP) systems have been proposed in the literature [3, 4]. Among the different proposed propulsion systems turboelectric architectures have been drawing attention due to many factors. When alone, turboelectric propulsion systems are less efficient than conventional configurations. However, they can be combined with Boundary Layer Ingestion (BLI) and distributed propulsion systems in order to create highly energy efficient configurations [5].

In the BLI design the jet and wake are located in the same axis, resulting in less noise and drag and, consequently, increasing the aircraft's energy efficiency [4]. Hence, a turboelectric architecture strikes a nice balance between fuel burn reduction, power/energy density, and technological readiness level, hence becoming the most attractive topology for more electric powertrains in the short term[6].

A potential turboelectric propulsion system configuration of an MEA is depicted in Figure 1. Note that the structure allows for the generator to be indirectly connected to the motor, meaning that the two AC systems have certain independent controls and resulting in increased operation flexibility overall. However, there are plenty different ways to assemble the AC/DC/AC system, depending on many aspects of the AC/DC/AC system.

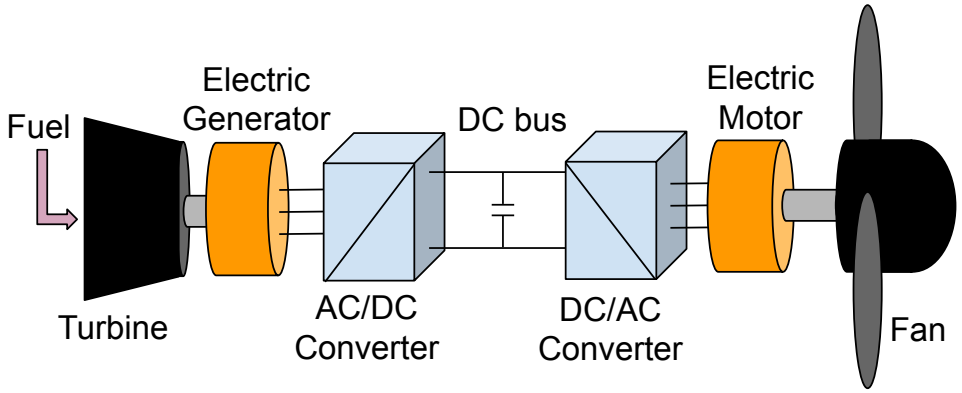

Fig. 1 General architecture example for a full turboelectric propulsion system.

At the component level, for example, different types of components can be integrated to fulfill the functionality of the electric propulsion branch: delivering electric propulsive power. For instance, AC power sources, such as a Field Controlled Synchronous Generator (FCSG) or a Permanent Magnet Synchronous Generator (PMSG), can be used as a generation unit. At the load side, synchronous reluctance machine, induction machine, or Permanent Magnet Synchronous Motor (PMSM), etc. can be used. In this study, the electric motor is always considered to be the PMSM, due to its higher efficiency and power density if compared to other alternatives such as induction motors [1].

At the system level, the turboelectric architecture herein allows the generator to be indirectly connected to the motor through controllable power electronics. However, there are other alternatives to assemble the AC-to-DC-to-AC system depending on the type of power electronics used to perform AC/DC and DC/AC conversions. By investigating different design options, guidelines to inform the system integration process could be established, helping engineers in the design process of turboelectric propulsion systems. The turboelectric architecture depicted on Figure 1, although seemingly simple, offers a variety of design options. The goal of this paper is to explore specific design options within

the architecture and understanding their pros and cons. The different configurations together with some parameter values were determined in a 0-D sizing procedure that is not detailed in this paper and will be subject of a future publication.

In the model-based design paradigm, the dynamics of Electric Power System (EPS) are modeled and simulated for assessment of both steady state and transient behavior, and Modelica solutions are one of the main alternatives for the modeling and simulation of MEA's EPS [1, 7]. Modelica is an acasual equation-based object-oriented language that allows the representation of dynamic systems without requiring modelers to specify the direction for the flow of computation, i.e. equations do not describe assignment statements (i.e. causality) but equality. The model, which is decoupled from the simulation tool, is analyzed by the software's transpiler, automatically generating C code that discretizes the model with a numerical solver selected by the user, compiled and then executed by the computer [8]. The resultant causalized model has a relatively small amount of algebraic loops, allowing the systems to be simulated more efficiently.

The advantages of Modelica and tools that support it make it ideal to study the different turboelectric propulsion architectures in this paper. The component models that are used to assemble the different turboelectric architectures are especially developed for this task. In addition, because EPS involves multiple time scales, which leads to heavy computation in simulation validation, special care should be exerted during the development of system model and the selection of simulation platform. In this study, the $dq-$frame modeling approach is adopted for simulation efficiency [2].

B. Goals and Objectives

Given this context, the present study serves a three-fold purpose:

1) to develop Modelica models and simulation packages to facilitate the analysis of turboelectric propulsion systems;
2) to assess the dynamic performance, also known as 1-D assessment, of different turboelectric propulsion architectures using the developed Modelica models; and
3) to assess Modelica as a tool for analyzing different turboelectric architectures while presenting the implementation of the component models.

C. Paper Organization

The remainder of this paper is organized as follows: Sections III and IV present the mathematical formulation and Modelica implementation of the different models representing machines and power electronic converters, respectively, which are used to compose the studied turboelectric architectures. Section V presents the control strategies that are used in the different systems assessed. Section VI presents the modeling of the flight mission as a load curve to the studied turboelectric propulsion system. Section VII depicts the different studied systems which are implemented in a digital simulation environment, while Section VIII present relevant simulation results. Final discussion and concluding remarks are presented in Section IX.

III. Modeling and Implementation of Electrical Machines

In this section, the mathematical models in $dq-$frame are described for the electromechanical components that are needed for assembling the different architectures that are assessed in this paper. They are used to represent the electrical generator and motor that are part of the turboelectric architecture as shown in Figure 1. In addition to the specific set of differential equations that govern their dynamic behavior, the Modelica implementation is also shown.

A. Permanent Magnet Synchronous Motor

The terminal voltages v_{dq0} in the Park reference frame for a surface-mounted PMSM are described in below [2]:

$$\begin{cases} v_d &= R_s i_d - \omega_e \lambda_q + \dfrac{d}{dt}\lambda_d, \\ v_q &= R_s i_q + \omega_e \lambda_d + \dfrac{d}{dt}\lambda_q, \\ v_0 &= R_s i_0 + \dfrac{d}{dt}\lambda_0, \end{cases} \tag{1}$$

where R_s represents the winding resistance, $\omega_e = 2\pi f_e$ is the electrical angular speed, i_{dq0} are the $dq0-$currents flowing into the machine, and λ_{dq0} are the flux linkages for $dq0-$axes, which are defined by Equation (2). Note that a variable written as x_{dq0} represents a vector with three variables, $\left[x_d, x_q, x_0\right]$ whereas x_{dq} is a vector with two variables $\left[x_d, x_q\right]$.

Observe that mechanical speed and the electrical speed are proportional as in $\omega_e = p\omega_m$, where ω_m is the mechanical speed and p is the number of pole pairs of the machine. Meanwhile, the flux linkages can be determined from

$$\begin{cases} \lambda_d &= (L_{md} + L_{ls})\, i_d + \lambda_m = L_d i_d + \lambda_m, \\ \lambda_q &= \left(L_{mq} + L_{ls}\right) i_q = L_q i_q, \\ \lambda_0 &= L_{ls} i_0 = L_0 i_0, \end{cases} \tag{2}$$

where λ_m is the magnetic flux coming from the permanent magnet, $L_{m,dq}$ are the $dq-$axes magnetizing inductance values and L_{ls} are the leakage inductance. In addition to that, the balance between electrical and mechanical torques is defined by

$$J\frac{d}{dt}\omega_m = T_e - T_L = \frac{3}{2}p\left[\lambda_m i_q + (L_d - L_q) i_d i_q\right] - T_L, \tag{3}$$

where J is the total moment of inertia of the motor, T_e is the electrical torque, and T_L is the mechanical load torque. The Modelica model of the PMSM can be separated into two parts: the electrical and the mechanical. The former can be declared in form of equations as shown below. It is important to note that variables `v_d`, `v_q`, `v_0` and `ground` are physical ports representing the electrical nodes. For each node `x`, it should be possible to measure two properties, `x.v` and `x.i`, representing voltage and current, respectively.

Listing 1 Modelica equations for the electrical part of the PMSM model.

```
equation
  vd = v_d.v - ground.v "Measuring d-voltage";
  vq = v_q.v - ground.v "Measuring q-voltage";
  v0 = v_0.v - ground.v "Measuring 0-voltage";
  iq = v_q.i "Measuring q-current";
  id = v_d.i "Measuring d-current";
  i0 = v_0.i "Measuring 0-current";
  ground.i = v_q.i + v_d.i + v_0.i "Connecting ground current";
  vd = Rs*id - p*measured.w*Lambda_q + der(Lambda_d) "d-voltage equation";
  vq = Rs*iq + p*measured.w*Lambda_d + der(Lambda_q) "q-voltage equation";
  v0 = Rs*i0 + der(Lambda_0) "0-voltage equation";
  Lambda_d = Ld*id + Lambda_m "d-flux linkage equation";
  Lambda_q = Lq*iq "q-flux linkage equation";
  Lambda_0 = L0*i0 "0-flux linkage equation";
  Te = (3/2)*p*(Lambda_m*iq + (Ld - Lq)*id*iq) "Electrical torque";
```

The mechanical equations can be declared in the PMSM model by the use of rotational mechanical components from the Modelica Standard Library (MSL). The electrical torque T_e acts in a rotational body with the motor's moment of inertia as it is shown in Figure 2. The connector named Flange A can then be connected to another mechanical device that will produce the torque on the opposing direction, such as the Fan depicted in Figure 1.

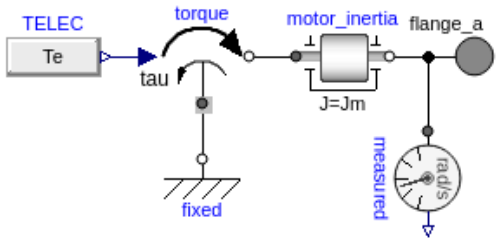

Fig. 2 Modelica diagram for the mechanical equations of a PMSM.

B. Permanent Magnet Synchronous Generator

The PMSG has a similar structure if compared to the PMSM. In fact, if the currents are considered to be entering the generator's terminal, then (1) are the same in PMSG equations. The difference is that a generator takes the energy from the shaft and transforms it into electrical energy. This energy flow results in the following electromechanical swing equation

$$J\frac{d\omega_m}{dt} = T_G - T_e = T_G - \frac{3p}{2}\left(\lambda_q i_d - \lambda_d i_q\right) \tag{4}$$

where T_G is the torque applied in the shaft by the generator's primary mover, such as turbofan engine. Therefore, the Modelica model representing the electrical circuit is the same as the one shown in Listing 1 and the only difference between the PMSG and the PMSM would be the implementation of the swing equation, resulting in a slightly different diagram as the one shown in Figure 2. In fact, in the generator, instead of `Te` one would find `-Te`.

C. Field Controlled Synchronous Generator

The most common type of synchronous generator is one where the magnetic field is generated by the rotor's field winding that is powered by an external DC source (e.g. a rectifier). FCSG allows the magnetic excitation to be controlled. The simplified circuits for both d and q axes, with their respective damping windings, can be drawn as shown in Figure 3 [2]. Note that the field circuit appears on the left-hand side of the d-axis circuit and, by controlling that voltage source, the current i_f allows control over an excitation flux, enabling the regulation of terminal voltage v_{dq} by control of d-axis component of voltage.

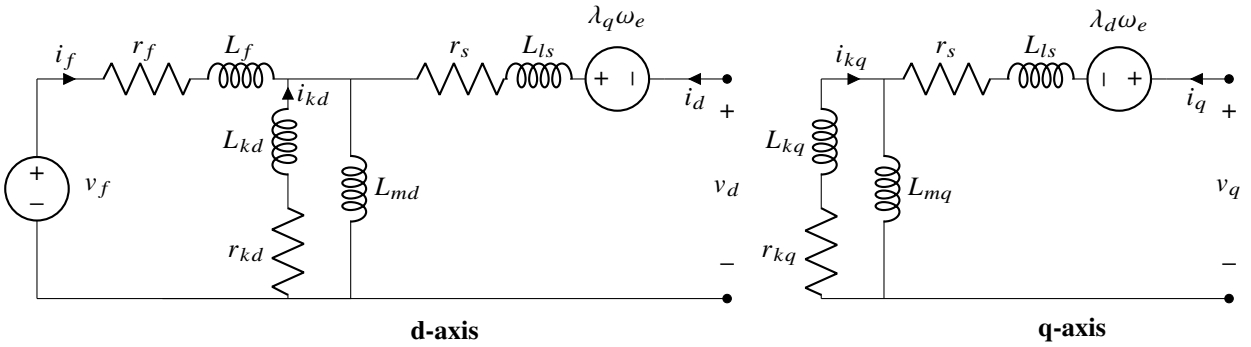

Fig. 3 Diagram representation for the dq-axis' electrical circuits of the FCSG model that is used in this study.

From Figure 3, if the d-axis circuit is divided into two loops it is possible to derive the differential set of equations as follows

$$\begin{cases} v_f &= r_f i_f + L_f \dfrac{d}{dt} i_f + L_{md} \dfrac{d}{dt}(i_d + i_f + i_{kd}), \\ v_d &= -\omega_e \lambda_q + r_s i_d + L_d \dfrac{d}{dt} i_d + L_{md} \dfrac{d}{dt}(i_f + i_{kd}), \\ v_q &= \omega_e \lambda_d + r_s i_q + L_q \dfrac{d}{dt} i_q + L_{md} \dfrac{d}{dt} i_{kd}. \end{cases} \tag{5}$$

where $L_q = L_{ls} + L_{mq}$ and $L_d = L_{ls} + L_{md}$. Meanwhile, the fluxes are determined by

$$\begin{cases} \lambda_d = L_d i_d + L_{md}(i_f + i_{kd}), \\ \lambda_q = L_q i_q + L_{mq} i_{kq}. \end{cases} \tag{6}$$

In addition to the circuit equations, the swing equation for the FCSG model is the same as the one shown in Equation (4). The only difference would be the fluxes λ_d and λ_q that are calculated differently depending on the generator model being analyzed. In order to show the versatility of the Modelica language, the FCSG model representation is built using the electrical components available in the Modelica Standard Library (MSL), as depicted in Figure 4. Complementing the diagram in describing the FCSG model, it is also useful to present the equations that are written in the `Text` layer of

the model. As one can see in Listing 2, the electrical torque as well as the electromagnetic fluxes are all calculated in that layer of the model.

Listing 2 Modelica equations for the FCSG model.

```
equation
  v_0.v = 0 "voltage in 0-sequence";
  we = p * measured.w "electrical frequency";
  iq = v_q.i "Measuring q-current";
  id = v_d.i "Measuring d-current";
  ikq = -damp_Lkq.i "Measuring damping q-current";
  ikd = -damp_Lkd.i "Measuring damping d-current";
  ifd = Efd_p.i "Measuring ifd current";
  lambdaQ = Lq * iq + Lmq * ikq "Induced q-axis magnetic flux";
  lambdaD = Ld * id + Lmd * (ifd + ikd) "Induced d-axis magnetic flux";
  emf_q = lambdaQ * we "Induced q-axis volage";
  emf_d = lambdaD * we "Induced d-axis volage";
  Te = 3 / 2 * p * (lambdaQ * id - lambdaD * iq) "Electrical torque";
```

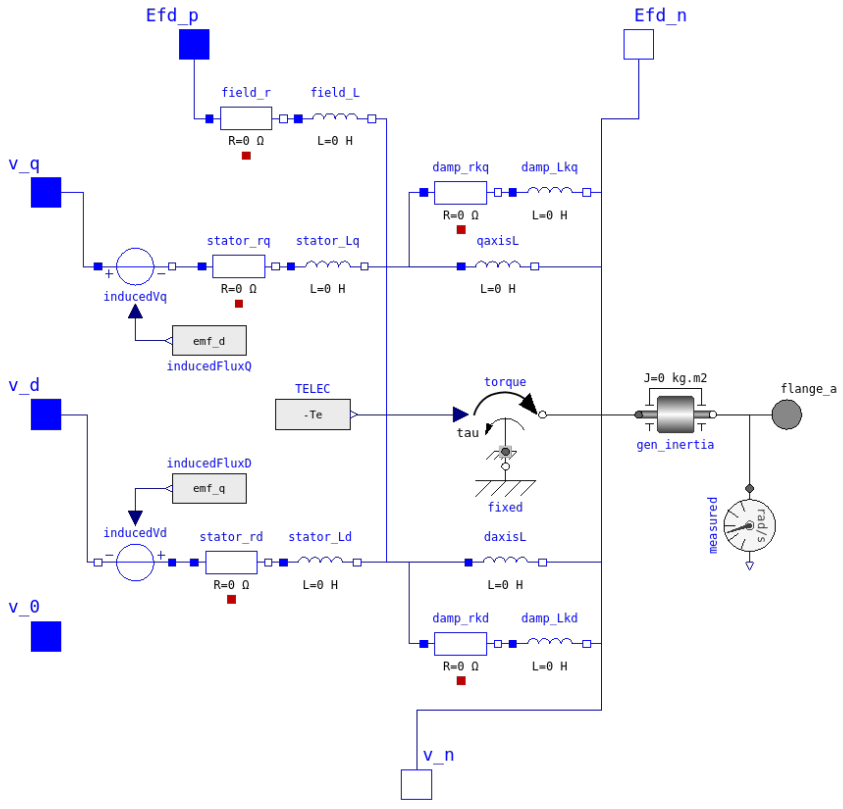

Fig. 4 Modelica diagram for the FCSG with damping windings.

IV. Modeling and Implementation of Power Electronic Converters

In this section, the Power Electronic Converters (PECs) that are used to interface the AC and DC systems are presented together with their mathematical model and their respective Modelica implementation. Two converters are modeled herein, the Voltage-Sourced Converter (VSC) and the 6-pulse diode bridge. The former can act as both rectifier

and inverter, while the latter can only be used as a three-phase rectifier. In addition, since all the machines are modeled in the dq-frame, and control strategies for the converters can be more easily implemented when in the $dq-$frame [9], the converters in this study are also modeled in that reference frame.

A. Voltage-Sourced Converters

One common architecture of a VSC is the two-level converter, which is composed of three half-bridge converters, one for each phase [9]. The converter's switching device is a full-controllable bi-directional cell composed of an IGBT connected in anti-parallel with a diode [9]. The full-switching model of a three-phase VSC can be averaged and then converted to the $dq-$frame by Clarke-Park transformation, yielding Equations (7) [9], which describes the relationship among the converter's terminal voltages, the DC current, and the modulation indices. If the converter is connected using the full-bridge architecture, i.e. there is no mid-point access in the DC bus, equations are slightly different and $\frac{V_{DC}}{2}$ would be replaced by $\frac{V_{DC}}{\sqrt{3}}$.

$$\begin{cases} v_{T,q}(t) &= \dfrac{V_{DC}}{2} m_q(t), \\ v_{T,d}(t) &= \dfrac{V_{DC}}{2} m_d(t), \\ I_{DC}(t) &= -\dfrac{3}{2V_{DC}} \left(v_{T,q} i_q + v_{T,d} i_d\right) = -\dfrac{3}{4} \left(m_q i_q + m_d i_d\right). \end{cases} \tag{7}$$

where $v_{T,dq}$, m_{dq} and i_{dq} are the converter's terminal phase voltages, modulation indices and terminal phase currents in dq coordinates, respectively. Moreover, V_{DC} and I_{DC} are the DC bus voltage and current respectively. Using all these equations and assuming $v_{T,0} \equiv 0$, it is possible to draw an implementation in Modelica that resembles Figure 5. The heat port shown in red can be used to interface the converter's heat flow with a thermal management system.

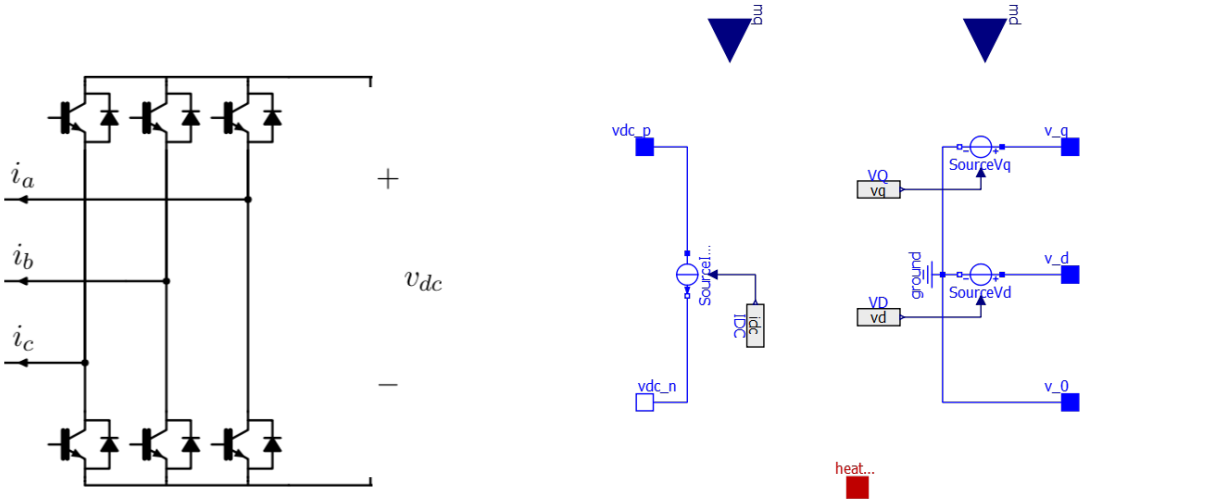

(a) Diagram representing a three-phase VSC. **(b) Averaged implementation of the dq VSC in Modelica.**

Fig. 5 A comparison between the three-phase VSC diagram in abc-frame and its dq-frame implementation in Modelica

Because of the full controllability feature of this converter it can be used with permanent magnet machines in order to allow for the regulation of important variables. When performing DC-to-AC conversion, this converter can be use to control the electric motor's torque and speed, for example. On the other hand, when performing AC-to-DC conversion, this converter can be used with the PMSG, regulating the reactive power on the generator at the same time that DC bus voltage level is controlled.

B. Six-Pulse Diode Bridge Rectifier

The six-pulse bridge, when assembled using diodes as its building blocks, is an uncontrollable rectifier, meaning that its output DC bus voltage is a direct consequence of the voltage waves' amplitude on its AC terminal. This is due to

the fact that the diode is an uncontrollable semiconductor device, meaning that the current flowing through it, i_D and the voltage over it, v_{AK}, cannot be controlled by an external device. In fact, these two variables have their behavior completely determined by the polarity of its current and voltage [10].

Given this fact, the relationship between AC voltage amplitude and the DC bus voltage output can be simplified to a simple gain constant. Since the AC terminal is modeled using dq-frame coordinates and assuming that a invariant-amplitude Park transformation is used [9], then it is possible to write Equation (8) [11]:

$$V_{DC} = \frac{3\sqrt{3}}{\pi}\sqrt{v_d^2 + v_q^2}, \tag{8}$$

where v_{dq} are the dq-frame components of the voltage waves in the rectifier's AC terminal. Moreover, the AC currents resulting from this transformation would be in-phase with respective AC voltages, meaning that the Park reference-frame transformation angle, θ_{dq}, used in voltage variables would also be used in the current variable. In addition, it is necessary to find the peak wave amplitude, in order to calculate the resulting dq-frame values for the current. This is done by simple multiplication as shown in Equation (9) [11].

$$\begin{cases} i_q = \dfrac{2\sqrt{3}}{\pi} I_{DC} \sin\theta_{dq}, \\ i_d = \dfrac{2\sqrt{3}}{\pi} I_{DC} \cos\theta_{dq}. \end{cases} \tag{9}$$

where I_{DC} is the magnitude of the stationary current flowing in the DC terminal of the converter. This set of equations can be implemented in Modelica following what is shown on Listing 3.

Listing 3 Modelica equations for the a Park frame six-pulse diode bridge rectifier.

```
equation
  vq = v_q.v - v_0.v "measuring q-axis voltage";
  vd = v_d.v - v_0.v "measuring d-axis voltage";
  Vdc = dc_p.v - dc_n.v "measuring dc-bus voltage";
  dc_n.v = 0 "setting voltage reference";
  vdq = sqrt(vd ^ 2 + vq ^ 2) "voltage magnitude";
  theta = asin(vd/vdq) "Park frame transformation angle";
  Idc = dc_p.i "measuring dc-bus current";
  iq = v_q.i "stating q-axis current";
  id = v_d.i "stating d-axis current";
  i0 = v_0.i "stating 0-axis current";
  Vdc = 3*sqrt(3)/Modelica.Constants.pi*vdq "calculating vdc";
  id = -sqrt(3)*2/(Modelica.Constants.pi)*sin(theta)*Idc "d-axis current";
  iq = -sqrt(3)*2/(Modelica.Constants.pi)*cos(theta)*Idc "d-axis current";
  i0 = 0 "0-axis current";
```

Because this converter is not controllable, it means that the voltage regulation on its DC terminal can be indirectly controlled by the AC terminal's voltage amplitude. Therefore, if a constant DC-bus voltage is desirable, the six-pulse diode bridge should be associated with FCSG, which should have its own terminal voltage regulation. Then, this excitation system can be used control the DC bus voltage.

V. Modeling and Implementation of Controllers

A. Motor Control

A VSC is connected to the PMSM in order to control its speed. Considering that the PMSM is surface-mounted, i.e. $L_d = L_q = L$, and considering that all states can be properly measured or estimated, it is possible to use a state feedback law for control. The controller's inputs of this model are the modulation indices of the VSC actuating as an inverter and are defined as in Equation (10).

$$\begin{cases} m_d = \dfrac{\kappa}{V_{DC}} \left[R_s i_d - L p \omega_m i_q - K_d L (i_d - I_d^*) \right], \\ m_q = \dfrac{\kappa}{V_{DC}} \left[R_s i_q + L p \omega_m i_d + p \omega_m \lambda_m - K_q L (i_q - I_q^*) \right]. \end{cases} \tag{10}$$

where K_{dq} is the control gain in dq coordinates, I^*_{dq} is the reference current for $dq-$axes and $\kappa = 2$ if the converter is half-bridge or $\kappa = \sqrt{3}$ if the converter is full-bridge. Furthermore, if Equation (10) is replaced in (7) and the terminal of the VSC is connected to the PMSM's terminal, that is, $v_{T,dq} = v_{dq}$, it is possible to simplify the motor's dynamic equations into the set presented in Equation (11).

$$\begin{cases} \dfrac{di_d}{dt} &= -K_d(i_d - I^*_d), \\ \dfrac{di_q}{dt} &= -K_q(i_q - I^*_q). \end{cases} \tag{11}$$

Note that K_d and K_q became the eigenvalues for i_d and i_q, respectively. In addition, if λ^*_d, T^*_L and ω^*_m are the nominal values for the $d-$axis magnetic flux, load torque and mechanical speed, respectively, it is possible to write that

$$I^*_d = \frac{\lambda^*_d - \lambda_m}{L}, \tag{12}$$

$$I^*_q = \frac{2}{3p\lambda_m}\left[T^*_L - K_\omega pJ\left(\omega_m - \omega^*_m\right)\right]. \tag{13}$$

If K_q is appropriately larger than K_ω, the $q-$axis controller is able to track the reference value I^*_q such that $T_L \approx T^*_L$. Hence, it is possible to consider that the swing equation for the controlled model becomes (14). Therefore, all three states from the PMSM can be controlled via the the terminal voltages of the inverter.

$$\frac{d}{dt}\omega_m = \frac{3\lambda_m}{2J}I^*_q - \frac{T_L}{Jp} = -K_\omega\left(\omega_m - \omega^*_m\right). \tag{14}$$

The value for the gains used in this study are $K_d = K_q = 100$ while $K_\omega = 10$. Meaning that the current control loop is set to be approximately 10 times faster than the speed control loop.

B. DC-Bus Voltage Control via Voltage-Sourced Rectifier

If a VSC is used to perform the interface between a PMSG and the DC bus, the converter is connected to the permanent magnet machine through a filter. This filter is, usually, an LCL filter but, if the capacitor is selected adequately, its dynamic behavior can be approximated to an RL branch [9]. Given this approximation, considering that reference currents flow out of VSC terminals, and that the system is in $dq-$frame, it is possible to write that [9, 12]:

$$\begin{cases} v_{T,q} - v_{s,q} = Ri_q + L\dfrac{di_q}{dt} + L\omega i_d, \\ v_{T,d} - v_{s,d} = Ri_d + L\dfrac{di_d}{dt} - L\omega i_q, \end{cases} \tag{15}$$

where $v_{s,d}, v_{s,q}$ are the voltages of the PMSG, R is the resistance and L is the inductance of the RL filter. If the reference currents flow from the PMSG into the VSC terminals, then the dynamics are given by

$$\begin{cases} L\dfrac{di_q}{dt} = -Ri_q - L\omega i_d + v_{s,q} - v_{T,q}, \\ L\dfrac{di_d}{dt} = -Ri_d + L\omega i_q + v_{s,d} - v_{T,d}. \end{cases} \tag{16}$$

As far as the control design is concerned, assume that all signals involved in the equation, i.e. $i_d, i_q, v_{d,s}, v_{q,s}, \omega$, are measured or estimated. Then, the VSC's terminal voltages can be designed to regulate i_d to i^*_d, and i_q to i^*_q. In fact, letting the terminal voltages be given by

$$\begin{cases} v_{T,q} = -Ri_q - L\omega i_d + v_{s,q} + K_q L(i_q - I^*_q), \\ v_{T,d} = -Ri_d + L\omega i_q + v_{s,d} + K_d L(i_d - I^*_d), \end{cases} \tag{17}$$

then, Equations (16) can be re-written as

$$\begin{cases} L\dfrac{di_q}{dt} = -Ri_q - L\omega i_d + v_{s,q} - \left[-Ri_q - L\omega i_d + v_{s,q} + K_q L(i_q - I^*_q)\right], \\ L\dfrac{di_d}{dt} = -Ri_d + L\omega i_q + v_{s,d} - \left[-Ri_d + L\omega i_q + v_{s,d} + K_d L(i_d - I^*_d)\right], \end{cases} \tag{18}$$

which, similar to Equation (11), can be further simplified into

$$\begin{cases} \dfrac{di_d}{dt} = -K_d(i_d - I_d^*), \\ \dfrac{di_q}{dt} = -K_q(i_q - I_q^*). \end{cases} \tag{19}$$

Meanwhile, the modulation corresponding to the terminal voltages in Equation (17) are given by

$$\begin{cases} m_q = \kappa \dfrac{v_{T,q}}{V_{DC}}, \\ m_d = \kappa \dfrac{v_{T,d}}{V_{DC}}. \end{cases} \tag{20}$$

Reference currents I_d^* and I_q^* can be calculated in an outer dynamic loop that can be designed for the control of voltage magnitude and DC capacitor voltage. In this system, consider that no control over the AC terminal voltage of the PMSG is applied, hence, $I_d^* = 0$. In addition, the q-axis current reference can be calculated for controlling the DC bus voltage by using

$$I_q^* = \frac{2\kappa}{3m_q}\left[I_{DC} - K_v C_{DC}\left(v_{DC} - V_{DC}^*\right)\right]. \tag{21}$$

This last equation can be used by the outer loop to control the DC link voltage if some conditions are met. For example, the speed of the current loop should be much faster than the time constant governing the DC voltage dynamics. Hence, if $K_q, K_d >> K_v$ it is possible to write the following dynamics for the capacitor voltage

$$\begin{aligned} C_{DC}\frac{d}{dt}v_{DC} &= -\frac{3m_d i_d}{2\kappa} - \frac{3m_q i_q}{2\kappa} + I_{DC} = -\frac{3m_q I_q^*}{2\kappa} + I_{DC}, \\ &= -\frac{3m_q}{2\kappa}\frac{2\kappa}{3m_q}\left[I_{DC} - K_v C_{DC}\left(v_{DC} - V_{DC}^*\right)\right] + I_{DC}, \end{aligned} \tag{22}$$

which would result in the first order dynamics presented in Equation (23).

$$\frac{d}{dt}v_{DC} = -K_v\left(v_{DC} - V_{DC}^*\right). \tag{23}$$

For this control system, $K_d = K_q = 250$ while $K_v = 50$, meaning that the current control loop is set to be approximately 5 times faster the DC bus control loop.

C. FCSG Terminal Voltage Control

The terminal voltage control of the FCSG is carried out by controlling the current that flows through the excitation field [13]. This is done indirectly, by controlling the voltage over the field circuit. In this study, the terminal voltage is compared to a reference value, that should be calculated in a way it ensures that the DC voltage output of the six-pulse diode bridge is kept constant in the desired value for a normal operation of the entire turboelectric system.

The basic dynamics behind the terminal voltage regulation are shown in the diagram depicted in Figure 6a. There, the reference terminal voltage is calculated via a simple gain applied to the DC bus voltage reference value. The resulting voltage is then compared with the measured machine's terminal voltage, and the error is applied to the regulator's control system. The resulting field voltage is the input to the field circuit that has the field current as output, affecting the terminal voltage through the generator equations [13, 14]. The excitation system highlighted in green in Figure 6a can be represented, for example, as a simplification of the IEEE Type ST2A [15] without the load compensation branch or the inductance saturation effects. This system represents a static excitation system with a PEC that directly acts on the excitation field [13]. This excitation system is often employed in generators with large power ratings that need to comply with standard metrics for performance [16]. Hence, the system can represented by the diagram presented in Figure 6b.

The control system is implemented in Modelica using the diagram layer shown in Figure 7. Note that comparing the Modelica implementation and the diagrams displayed in Figure 6, there is one additional component that contributes to the variable e, representing the error between the reference and measured values. This is due to the fact that exciters usually work with an amplification of the error, meaning that, in steady state, $v_f = \frac{K_A}{K_E}e$. Although K_A is usually very

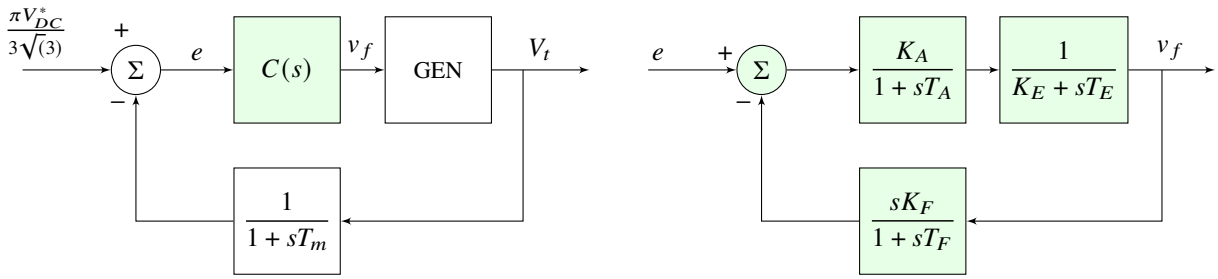

(a) Excitation and connection to a generator. **(b) Excitation control system for the FCSG.**

Fig. 6 Excitation effect over the terminal voltage of the FCSG and its control system diagram.

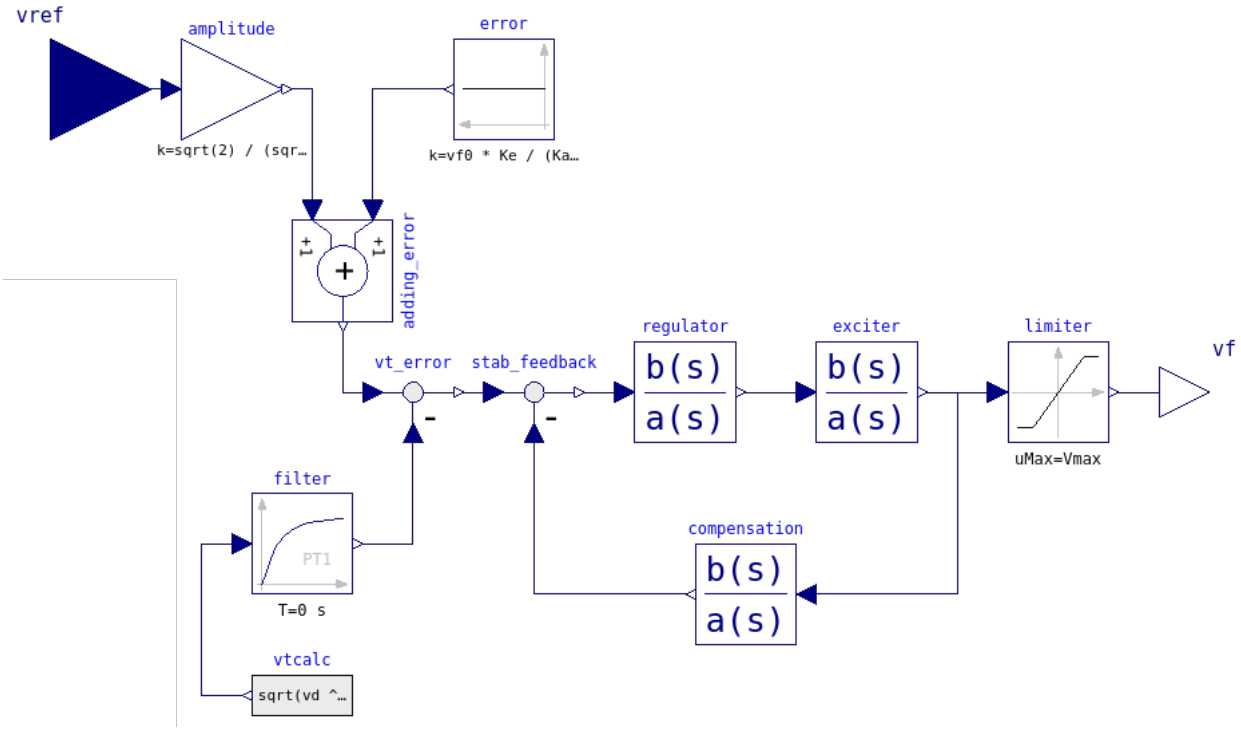

Fig. 7 Modelica implemntation of the excitation control system for the FCSG.

large, meaning that the error is indeed very small, some additional component compensates for such steady state error, making it zero during initial conditions. Another important observation that should be made is that excitation systems are often tuned using *per unit* values and, therefore, it is necessary to divide by the voltage base before the input e and then multiply by it after v_f.

In this study, the parameters used in terminal voltage control for the FCSG are summarized in Table 1.

VI. Flight Mission Profile Modeling

The flight mission profile is implemented in this study by the use of reference curves for speed, in the turbine side, and for speed and torque at the fan's side. The profile considers an example flight mission of 400 seconds and the reference curves are shown in Figure 8.

First, let us look at the turbine side, i.e. the dark solid curve in Figure 8. At $t = 0$ s., the generator is assumed to be spinning at its lowest nominal value of 5400 rpm or 360 Hz in the electrical frequency. At $t = 2$ s., the turbine is set to increase its speed, leading the electrical generator to increase its frequency to 800 Hz as in preparation for take-off. This

Table 1 Synchronous Generator Excitation System Parameters

Parameter	Description	Value	Unit
T_m	Measurement time constant	0.5	ms
K_A	Regulator gain	200	V/V
T_A	Regulator time constant	0.02	s
K_f	Stabilizer compensator derivative gain	0.001	s
T_f	Stabilizer compensator time constant	0.82	s
K_e	Exciter constant	1	V/V
T_e	Exciter time constant	0.021	s

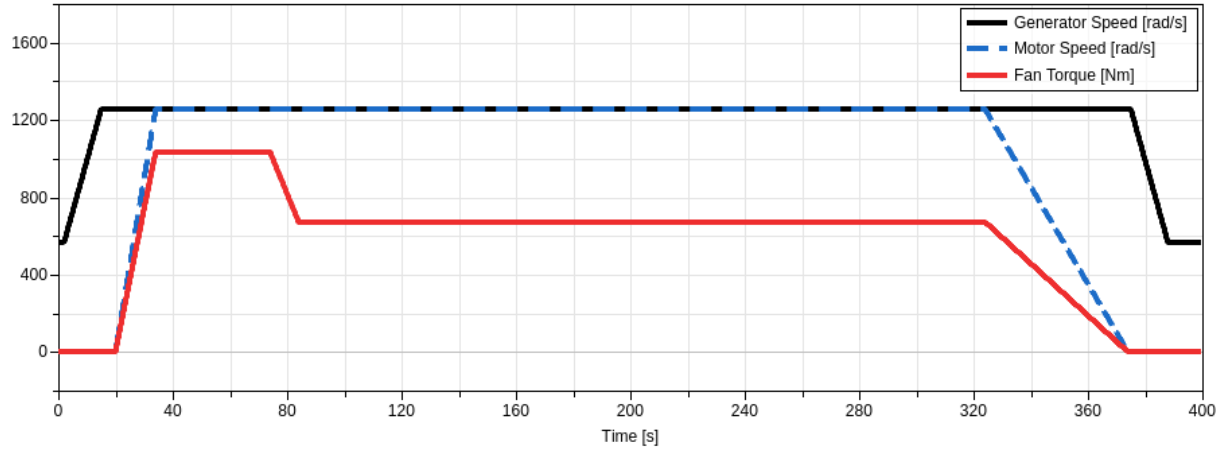

Fig. 8 Flight mission load profile for the electrical motor in terms of torque and speed, and for the electrical generator in terms of speed.

ramp-up procedure takes 13 seconds. After that, the generator's speed is maintained constant until $t = 375$ s. After the flight mission is completed, the generator's speed reference decreases to 5400 rpm, taking 13 s., and remaining at that value until the end of the simulation.

Now, looking at the fan side, there are two different curves, speed and torque in Figure 8. The curve in dashed blue is the motor's speed reference and it starts to increase at $t = 20$ seconds until it reaches the nominal speed of 5400 rpm. This process takes 14 s. and is used to represent the *take-off*. After that, during *climb* and *cruise*, the speed is maintained constant at 5400 rpm. Finally, at $t = 330$ s., the *descent and landing* part begins and the speed is reduced until it reaches 0, at $t = 380$ seconds. The fan torque curve, in solid red, also starts increasing at $t = 20$ s. until it reaches its maximum value of 1035 Nm, representing the *take-off* and taking 14 s. For the *climb* period, the torque remains at its maximum value for 40 s. After that, the torque diminishes until it reaches 65% of its maximum value, which is the torque needed for *cruise*. It remains at this value for 240 s., until it reaches $t = 330$ seconds, when the *descent and landing* part begins, reducing the torque to zero and taking 50 s.

VII. Studied Turboelectric Architectures

Two different examples of turboelectric systems are analyzed in this paper and their differences arise from the distinctive adoption of "Electrical Generator" and "AC/DC Converter", from Figure 1. The turbine and the fan (load) are all represented by sources of torque in Modelica, being directly influenced by the flight mission profile described in the previous section. However, it is important to notice that the developed models allow these torque sources to be replaced by detailed models of actual aircraft engines [17]. In all four cases, the generator is assumed to be connected to the turbine via a gearbox with a fixed ratio, instead of a Constant Speed Drive (CSD), to reduce the complexity of the mechanical system, following the practice adopted in the latest aircraft models like the Boeing 787 and the Airbus 380

[18]. Therefore, in all four cases, the generator operates under a Variable Speed Variable Frequency (VSVF) regime, meaning that the system's frequency changes proportionally to the engine's speed [1].

A. DC Link, Inverter and Motor

This sub-system is similar in both studied architectures and, therefore, it is described first. The DC link is composed by a capacitor with $C = 47\ \mu$F and a resistor $r_{DC} = 10$ mΩ used to represent cable thermal losses. The voltage value over the DC capacitor is different in each architecture depending on the adopted AC/DC converters and therefore, it will be specified in their own dedicated subsections. The VSI uses the control system and the parameters described in Subsection V.A and the parameters for the PMSM used in both architectures are described in Table 2.

Table 2 Permanent Magnet Synchronous Motor Parameters.

Parameter	Description	Value	Unit
r_s	Stator resistance	0.051	Ω
L_q	Quadrature axis inductance	0.5	mH
L_d	Direct axis inductance	0.5	mH
L_0	Zero axis inductance	0.5	mH
λ_m	Permanent magnet flux	0.46	Wb
J_M	Motor's moment of inertia	2.88	$Kg \cdot m^2$
ω_n	Nominal speed	360 – 800	Hz
p	Number of pairs of poles	4	–

B. Studied Architecture 1: PMSG and VSC

The first configuration has a PMSG as its electrical generator and a VSC acting as a rectifier. The reason behind this choice lies in the fact that PMSG has high efficiency and power density, therefore becoming advantageous to consider in such turboelectric architectures [6, 19]. The VSC is chosen due to its capability for DC bus voltage control by regulation of the modulation indices, as shown in Subsection V.B. These two components are interconnected via an RL filter, used to smooth the currents into almost-sinusoidal waves and, therefore, avoid jeopardizing the generator's expected performance due to harmonics. The Modelica diagram for this configuration is presented in Figure 9, where the electrical system together with its controllers and torque sources are all represented.

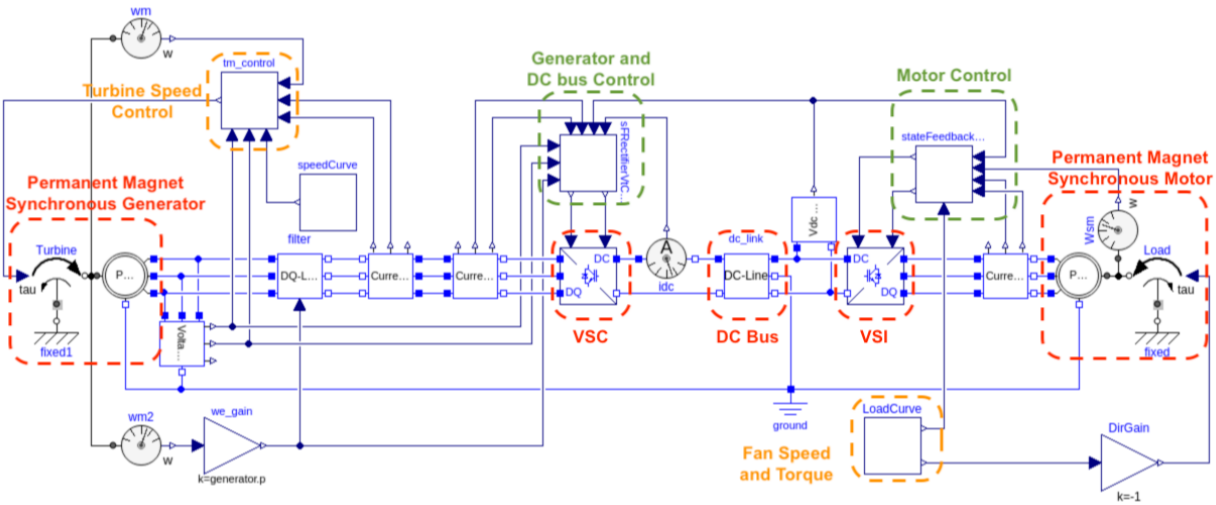

Fig. 9 Modelica implementation of the studied turboelectric systems with PMSG and VSC as rectifier.

The RL filter that is used to interface the PMSG and the VSC acting as a rectifier has resistance $r = 0.1$ mΩ and

inductor $L = 0.1$ mH. Besides that, the voltage over the DC link capacitor is 6 kV, which is much higher than the current practices. However, these values were chosen to accommodate a much higher power demand. This may be necessary in future turboelectric architectures to take advantage of higher efficiency at high power levels [6, 20, 21]. The VSC is connected in a full-bridge topology (i.e. $\kappa = \sqrt{3}$) and is controlled using the strategy presented in Subsection V.B, using the $K_d = K_q = 250$ and $K_v = 50$. The PMSG parameters are summarized in Table 3.

Table 3 Permanent Magnet Synchronous Generator Parameters

Parameter	Description	Value	Unit
R_s	Stator resistance	0.076	Ω
L_q	Quadrature axis inductance	0.8	mH
L_d	Direct axis inductance	0.8	mH
L_0	Zero axis inductance	0.8	mH
λ_m	Permanent magnet flux	0.56	Wb
J_G	Generator's moment of inertia	2.68	$Kg \cdot m^2$
ω_n	Nominal speed	360 – 800	Hz
p	Number of pairs of poles	4	–

C. Studied Architecture 2: FCSG and Diode Bridge

In the second architecture, the PMSG is replaced by the FCSG, which has its field current being controlled in order to guarantee that the terminal voltage is kept at its nominal value. Therefore, the FCSG is composed by a three stage machine [2] and the field current control system. Because the terminal voltage is controlled, the DC voltage is not expected to present large variations when a 6-pulse diode bridge is used as a rectifier. The diagram for this architecture is presented in Figure 10. Note that, in this case, because the diode rectifier is used, the nominal voltage for the DC bus is 3 kV.

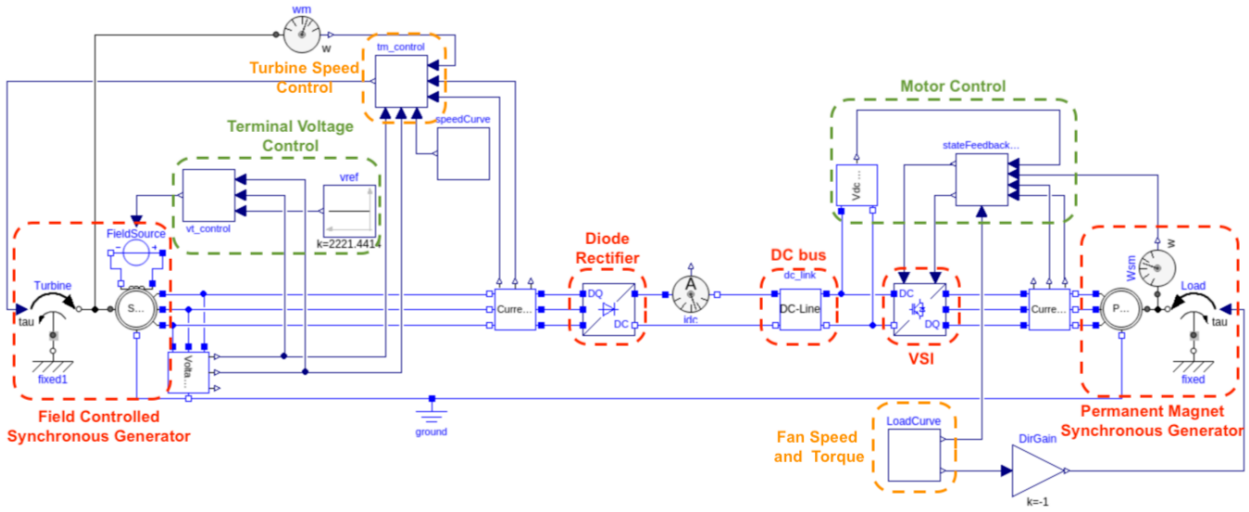

Fig. 10 Modelica implementation of the studied turboelectric systems with FCSG and diode bridge as rectifier.

The terminal voltage control is performed using the circuits and the parameters present in Subsection V.C. The parameters for the FCSG are summarized on Table 4.

VIII. Simulation Results

The simulation results presented in this section correspond to a 400−second simulation in Dymola®2021x running on a Ubuntu 20.04 machine with an Intel i7 processor with 8 cores @ 2.9 MHz and 16 GB of RAM. Simulation is done

Table 4 Field Controlled Synchronous Generator Parameters

Parameter	Description	Value	Unit
r_f	Field circuit resistance	0.076	Ω
L_f	Field circuit inductance	45	mH
r_s	Stator resistance	0.076	Ω
L_{ls}	Stator inductance	0.3	mH
L_{mq}	Quadrature axis magnetizing inductance	0.5	mH
L_{md}	Direct axis magnetizing inductance	0.5	mH
r_{kdq}	D and Q axes damping resistance	0.5	$m\Omega$
L_{kdq}	D and Q axes damping inductance	0.15	mH
J_G	Generator's moment of inertia	2.68	$Kg \cdot m^2$
ω_n	Nominal speed	$360 - 800$	Hz
V_t	Generator's terminal voltage (nominal)	2220	V
p	Number of pairs of poles	4	–

using the variable time-step DASSL solver [22], with tolerance equal to 10^{-6} and displaying 50 thousand points for each output curve. Architecture 1 has 565 DAE equations and unknowns and its simulation took 7.81 seconds, while Architecture 2 is compiled with 518 DAE unknowns and equations and it took 2.23 seconds to simulate. This is because the latter allows larger time steps during simulation, accelerating the numerical solution procedure.

A. Architecture 1:PMSG and VSC

The results for the variables related to the PMSG are depicted in Figure 11. Note that, since the control acting on the VSC aims to keep the $d-$axis current equal to zero and the DC-link voltage constant, the generator's terminal voltage, i.e. $\sqrt{v_d^2 + v_q^2}$, actually increases when the generator's speed increases. Recall that there is no excitation field control in a permanent-magnet-type machine. The lack of control for the generator's terminal voltage makes it difficult for other devices to be connected in the AC bus close to the generator, however, note that adequate reference values for $d-$axis current could ensure the generator's terminal voltage to be constant.

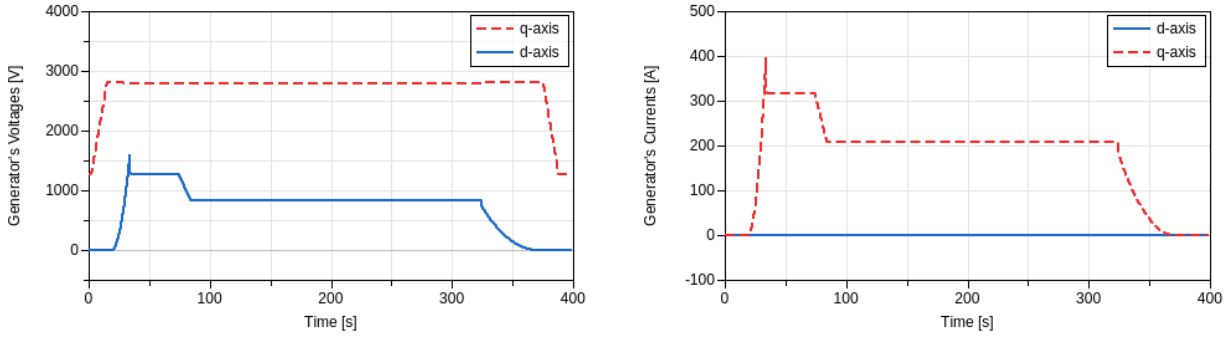

(a) Terminal voltages on PMSG. **(b) Terminal currents on PMSG.**

Fig. 11 Resulting PMSG terminal $dq-$frame currents and voltages.

The DC bus voltage is controlled by the $q-$axis current from the VSI and, as it is presented in Figure 12a, this task can be properly performed during the simulated flight mission. Note that the DC bus voltage varies less than 1% during the entire simulation. In addition, the motor currents are depicted in Figure 12b and it is possible to note similarities between $q-$axis currents from Figure 11b. This is because both AC systems are coupled in terms of active power, which could be controlled by $q-$axis current. However, the different behavior observed on $d-$axis current shows the decoupling between the two AC systems allowed by the AC/DC/AC configuration of the turboelectric architecture

studied here.

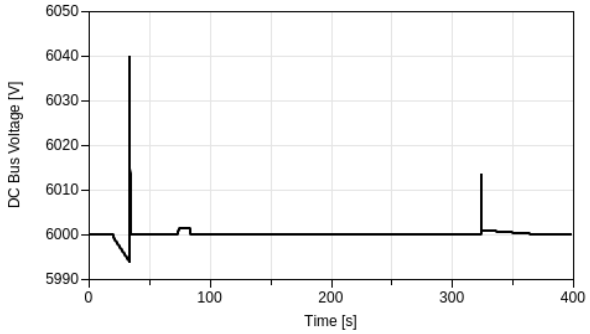

(a) Controlled DC bus voltage.

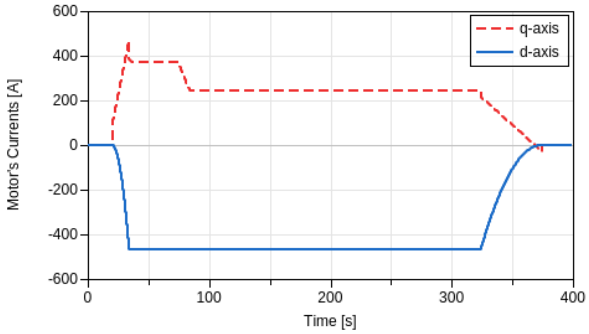

(b) PMSM terminal currents.

Fig. 12 DC bus voltage and terminal currents of PMSM for Architecture 1.

B. Architecture 2: FCSG and Diode Bridge

The results for the FCSG variables are presented in Figure 13. Note that, in this case, the $d-$axis current is not controlled to be zero and, therefore, it varies differently from what is presented in Figure 11b. Note also that the voltage over the field circuit varies in order to keep the generator's terminal voltage constant throughout the flight mission, therefore, while changing the DC bus voltage to provide the require terminal voltage.

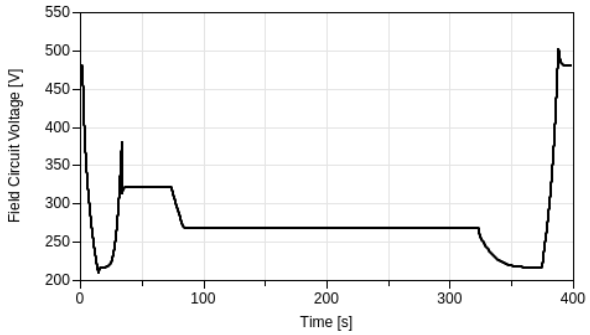

(a) Field circuit voltage on FCSG.

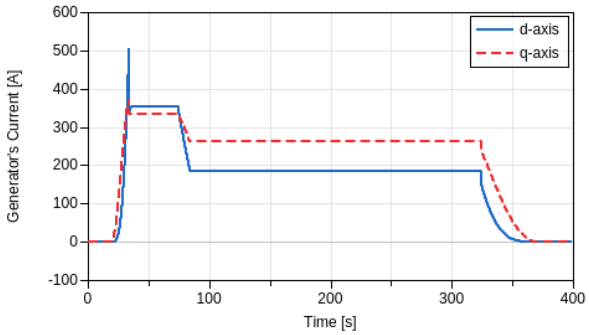

(b) Terminal currents on FCSG.

Fig. 13 Resulting FCSG field circuit voltage and terminal $dq-$frame currents.

The DC-bus voltage resulting from the simulation of the second architecture is presented in Figure 14a. Note that the voltage varies $\approx 4\%$ in the worst case scenario and, therefore, the terminal voltage control can be considered to be successful. Note also that the dynamic response depicted here is slower than the dynamic response observed in Figure 12a. This is because the FCSG regulates the DC bus voltage through a terminal voltage controller acting on its field winding, while the on the PMSG case, this control is executed by an IGBT-based power electronic converter. It is also important to highlight that different controllers can be additionally designed in order to improve this dynamic performance. The motor currents for this architecture are depicted in Figure 14b and it is possible to note that they are very similar to the results presented in Figure 12b, showing once again that, if variables are properly controlled, the performance of one side of the architecture does not affect the other. In this case, it is shown how the motor performance is almost independent from the type of generator and its controller as long as the DC bus voltage is properly controlled.

IX. Conclusion

This paper provides the dynamical models of various electrical devices, from synchronous machines to power electronic converters, in $dq-$frame, along with different controllers that are used to regulate these devices' dynamic

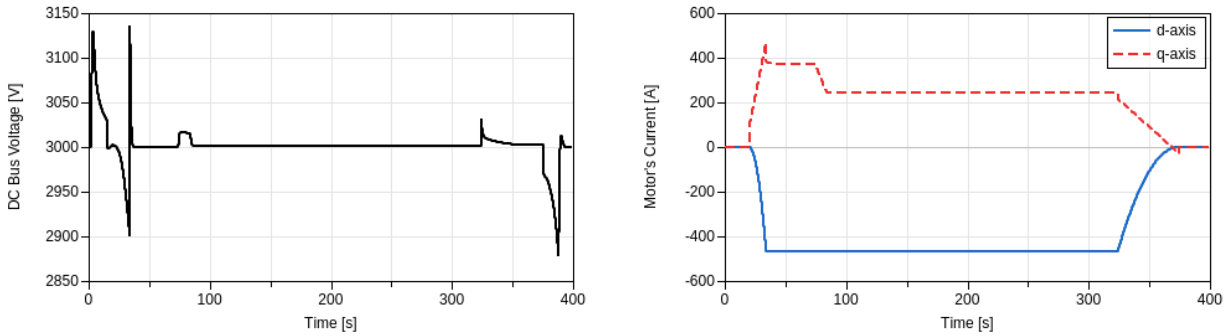

(a) Controlled DC bus voltage. **(b) PMSM terminal currents.**

Fig. 14 DC bus voltage and terminal currents for permanent magnet motor for Architecture 2.

behavior and their implementation in the Modelica language. The choice for the $dq-$frame allows fast dynamic simulation and analysis of relatively complex turboelectric propulsion architectures to be made. In addition, other simplifications can be exploited when the $dq-$frame is adopted, such as in the case of control design. In the results, it was shown that even the simulation of 400−second flight mission took, at most, 7.81 seconds to be simulated. The current paper illustrates how Modelica can be suitable for the study turboelectric architectures that are necessary for the development of more electric aircraft.

This study has also shown that transient stability performance must be taken into account when sizing the system and defining its parameters. For example, different DC voltages had to be used in the different turboelectric architectures due to the converter type chosen. Furthermore, it is possible to highlight challenges and strengths from studied each architecture. For instance, configurations with PMSG are lighter than the FCSG case, although they require a more complex power electronics converter to regulate DC bus voltage. On the other hand FCSG architectures allow the regulation of the generator's terminal voltage and DC bus voltage at their desired values with a simpler rectifier, however, the terminal voltage control might be more challenging and, if poorly designed, the controllers can lead the entire system to instability.

Future works include the analysis of better control strategies for different architectures, including more realistic models for the aircraft's engine [17] and fan. Furthermore, it is also important to study the impact of noise when applied to the flight mission profile and its effects over the architectures' dynamic performance.

References

[1] Sarlioglu, B., and Morris, C. T., "More electric aircraft: Review, challenges, and opportunities for commercial transport aircraft," *IEEE transactions on Transportation Electrification*, Vol. 1, No. 1, 2015, pp. 54–64.

[2] Bozhko, S., Hill, C. I., and Yang, T., "More-electric aircraft: Systems and modeling," *Wiley encyclopedia of electrical and electronics engineering*, 2018, pp. 1–31.

[3] Hall, D. K., Huang, A. C., Uranga, A., Greitzer, E. M., Drela, M., and Sato, S., "Boundary layer ingestion propulsion benefit for transport aircraft," *Journal of Propulsion and Power*, Vol. 33, No. 5, 2017, pp. 1118–1129.

[4] Kratz, J. L., and Thomas, G. L., "Dynamic analysis of the STARC-ABL propulsion system," *AIAA Propulsion and Energy 2019 Forum*, 2019, p. 4182.

[5] Gohardani, A. S., Doulgeris, G., and Singh, R., "Challenges of future aircraft propulsion: A review of distributed propulsion technology and its potential application for the all electric commercial aircraft," *Progress in Aerospace Sciences*, Vol. 47, No. 5, 2011, pp. 369–391.

[6] Benzaquen, J., He, J., and Mirafzal, B., "Toward more electric powertrains in aircraft: Technical challenges and advancements," *CES Transactions on Electrical Machines and Systems*, Vol. 5, No. 3, 2021, pp. 177–193.

[7] Bals, J., Ji, Y., Kuhn, M. R., and Schallert, C., "Model based design and integration of more electric aircraft systems using Modelica," *MOET forum at European power electronics conference and exhibition*, 2009, pp. 1–12.

[8] Bogodorova, T., Sabate, M., Leon, G., Vanfretti, L., Halat, M., Heyberger, J.-B., and Panciatici, P., "A modelica power system library for phasor time-domain simulation," *IEEE PES ISGT Europe 2013*, IEEE, 2013, pp. 1–5.

[9] Yazdani, A., and Iravani, R., *Voltage-Sourced Converters in Power Systems: Modeling, Control, and Applications*, John Wiley & Sons, 2010.

[10] Kassakian, J. G., Schlecht, M. F., and Verghese, G. C., *Principles of Power Electronics*, Vol. 1991, Addison-Wesley Reading, MA, 1991.

[11] Finotti, C., Gaio, E., Benfatto, I., Song, I., and Tao, J., "Continuous state-space model in dq frame of the thyristor AC/DC converters for stability analysis of ITER pulsed power electrical system," *IEEE Transactions on Plasma Science*, Vol. 44, No. 11, 2016, pp. 2923–2931.

[12] Krause, P. C., Wasynczuk, O., Sudhoff, S. D., and Pekarek, S. D., *Analysis of Electric Machinery and Drive Systems*, John Wiley & Sons, 2013.

[13] Kundur, P., *Power System Stability and Control*, CRC press New York, NY, USA, 2007.

[14] Chapman, S. J., *Electric Machinery Fundamentals*, McGraw-Hill, 2004.

[15] *IEEE Recommended Practice for Excitation System Models for Power System Stability Studies*, IEEE Standard 421.5, 1992.

[16] Nøland, J. K., Nuzzo, S., Tessarolo, A., and Alves, E. F., "Excitation system technologies for wound-field synchronous machines: Survey of solutions and evolving trends," *IEEE Access*, Vol. 7, 2019, pp. 109699–109718.

[17] Sielemann, M., Pitchaikani, A., Selvan, N., and Sammak, M., "The Jet Propulsion Library: Modeling and simulation of aircraft engines," *Proceedings of the 12th International Modelica Conference*, 2017, pp. 909–920.

[18] Wang, Y., Nuzzo, S., Zhang, H., Zhao, W., Gerada, C., and Galea, M., "Challenges and opportunities for wound field synchronous generators in future more electric aircraft," *IEEE Transactions on Transportation Electrification*, Vol. 6, No. 4, 2020, pp. 1466–1477.

[19] Zhang, X., Bowman, C. L., O'Connell, T. C., and Haran, K. S., "Large electric machines for aircraft electric propulsion," *IET Electric Power Applications*, Vol. 12, No. 6, 2018, pp. 767–779.

[20] Zhang, D., He, J., and Pan, D., "A megawatt-scale medium-voltage high-efficiency high power density "SiC+ Si" hybrid three-level ANPC inverter for aircraft hybrid-electric propulsion systems," *IEEE Transactions on Industry Applications*, Vol. 55, No. 6, 2019, pp. 5971–5980.

[21] He, J., Zhang, D., and Torrey, D., "Recent advances of power electronics applications in more electric aircrafts," *2018 AIAA/IEEE Electric Aircraft Technologies Symposium (EATS)*, IEEE, 2018, pp. 1–8.

[22] Petzold, L. R., "Description of DASSL: a differential/algebraic system solver," Tech. rep., Sandia National Labs., Livermore, CA (USA), 1982.